A Generalized Orthogonal Subspace Projection Approach to Unsupervised Multispectral Image Classification

Hsuan Ren, *Student Member, IEEE,* and Chein-I Chang, *Senior Member, IEEE*

***Abstract*—Orthogonal subspace projection (OSP) has been successfully applied in hyperspectral image processing. In order for the OSP to be effective, the number of bands must be no less than that of signatures to be classified. This ensures that there are sufficient dimensions to accommodate orthogonal projections resulting from the individual signatures. Such inherent constraint is not an issue for hyperspectral images since they generally have hundreds of bands, which is more than the number of signatures resident within images. However, this may not be true for multispectral images where the number of signatures to be classified is greater than the number of bands such as three-band pour l'observation de la terra (SPOT) images. This paper presents a generalization of the OSP called generalized OSP (GOSP) that relaxes this constraint in such a manner that the OSP can be extended to multispectral image processing in an unsupervised fashion. The idea of the GOSP is to create a new set of additional bands that are generated nonlinearly from original multispectral bands prior to the OSP classification. It is then followed by an unsupervised OSP classifier called automatic target detection and classification algorithm (ATDCA). The effectiveness of the proposed GOSP is evaluated by SPOT and Landsat TM images. The experimental results show that the GOSP significantly improves the classification performance of the OSP.**

***Index Terms*—Automatic target detection and classification algorithm (ATDCA), band generation process (BGP), band number constraint (BNC), desired target detection and classification algorithm (DTDCA), generalized orthogonal subspace projection (GOSP), intrinsic dimensionality constraint (IDC), orthogonal subspace projection (OSP), target classification process (TCP), target generation process (TGP).**

I. Introduction

HYPERSPECTRAL imagery differ from multispectral imagery in the sense that the former uses hundreds of contiguous bands to acquire data, while the latter uses only tens of discrete bands. As a result, hyperspectral imagery can discriminate and quantify materials more effectively in much narrower ranges than those used by multispectral imagery. But this also comes at a price that data volumes are substantially increased and general image processing techniques may not be adequate for such large dimensionality. In a recent work [1], Harsanyi and Chang developed an orthogonal subspace projection (OSP)-based classifier that not only could reduce dimensionality, but also showed success in hyperspectral image classification [2]–[5]. It was further shown to be an optimal linear classifier in terms of least squares error [5] and equivalent to the maximum likelihood classifier in [6], [7] with Gaussian noise assumption.

In order for the OSP to be effective, the intrinsic dimensionality (or true dimensionality of data) must be no less than the number of signatures to be classified. This constraint, referred to as the intrinsic dimensionality constraint (IDC), requires that the data should have sufficient dimensions to perform orthogonal subspace projection. In this case, each individual signature can be classified in a separate dimension for discrimination. In particular, the number of signatures to be classified cannot be greater than the total number of spectral channels (bands) used to acquire the data. The phenomenon of the IDC was first witnessed in [8]–[10], when the OSP was applied to three-band satellite pour l'observation de la terra (SPOT) data where four signatures were used for classification. It was found that the OSP performed poorly in discriminating four signatures using three-band SPOT data, particularly those with similar spectra [8]. More precisely, if we want to classify objects effectively using OSP, each object requires a separate dimension for orthogonal projection. If there is a dimension used to accommodate two or more objects, it is impossible to discriminate these objects using a single dimension through orthogonal projection. This constraint, referred to as band number constraint (BNC) was discussed in [8]. It points out an inherent limitation on the OSP. However, this problem does not seem to be an issue in hyperspectral data exploitation, since hyperspectral images generally have more bands than signatures resident within images, such as 224 bands for airborne visible/infrared imaging spectrometer (AVIRIS) data and 210 bands for hyperspectral digital imagery collection experiment (HYDICE) data. As a consequence, the significance of IDC has been overlooked in hyperspectral image processing. The finding in [8]–[10] leads to seeking a solution that can expand the capability of the OSP to multispectral image classification. However, finding the intrinsic dimensionality is generally a difficult problem and is considered to be very challenging. Rather than estimating the IDC directly, this paper considers a much simpler problem by dealing with the BNC. The relationship among the IDC, the BNC, and the number of signatures to be classified can be briefly described as follows.

One advantage of the BNC over the IDC is that there is no need to determine the intrinsic dimensionality. However, this is also traded for a disadvantage that the violation of IDC does not imply the violation of the BNC. If we let p, q, and l denote the

Manuscript received March 11, 1998; revised September 20, 1999.

The authors are with the Remote Sensing Signal and Image Processing Laboratory, Department of Computer Science and Electrical Engineering, University of Maryland Baltimore County, Baltimore, MD 21250 USA (e-mail: cchang@umbc.edu).

Publisher Item Identifier S 0196-2892(00)06224-0.

number of signatures to be classified, intrinsic dimensionality, and the number of bands, respectively. Obviously, $l \geq q$ and the IDC say that q must be greater than or equal to $p, (q \geq p)$, while the BNC states that l must be greater than or equal to p ($l \geq p$). It should be noted that since the OSP considered in this paper is an unconstrained linear unmixing method, it does not implement the sum-to-one constraint where the abundance fractions of all signatures must sum to one. So the BNC implies that $l \geq p$. However, if the sum-to-one constraint is imposed on the OSP [11]–[13], in this case, the BNC is replaced by $l \geq 1 + p$. So if the BNC is violated, so is the IDC, but not vice versa. In other words, it is possible that $l \geq p > q$, in which case the BNC is satisfied but the IDC is violated. The issue of the IDC or the BNC is also found in linear spectral mixture analysis where an inverse problem must be solved by an appropriate matrix rank [13]–[20]. A similar problem also occurs in sensor array processing where finding a number of signals arrived from an array of sensors presents a great challenge. There are many criteria proposed in the literature such as an information criterion (AIC) [21], [22], minimum description length (MDL) [22], [23], but most of them tend to overestimate the intrinsic dimensionality. Remotely sensed imagery has more complicated natural structures than the signals dealt in sensor array processing due to the nonstationary nature of image scenes and the various effects resulting from atmospheric scattering, topography, etc. Therefore, the criteria used for sensor array processing may not be applicable to remote sensing imagery. In recent attempts, a Neyman-Pearson approach [24] and a noise subspace approach [25] were proposed to determine the number and identity of spectral endmembers in hyperspectral imagery and has shown some success.

Two approaches were proposed in the past to alleviate the BNC [8]–[10]. One was to replace the OSP by a method, which combines the linear mixing with a Kalman filter (KFLM) [8]. This KFLM cannot be viewed as an extension nor a generalization of the OSP. Another approach reduced the number of signatures to be classified so that the BNC could be satisfied and the OSP could still be applied to multispectral imagery. But the results were not comparable to those obtained by the KFLM, as shown in [8]. Besides, the latter approach requires that all possible combinations of signatures be examined so that a best classification result could be selected for final classification. In this paper, we take an alternative approach. Instead of reducing the number of signatures as proposed in [8], we expand the original bands by creating a number of new bands. These new bands are generated nonlinearly in an attempt to capture nonlinear correlation between the original bands and can be used to improve classification performance. It is worth noting that linearly generated bands do not provide any useful information in linear mixture analysis. Incorporating these new nonlinearly correlated bands into original bands increases the number of bands to meet the BNC. The concept of creating correlated bands can be traced back to multivariate analysis, where a data correlation matrix is generally used to capture the second-order statistics of the data [26]. Recently, this idea was also applied to HYDICE data [27]. Due to significant improvement on spatial resolution (from 1 m to 4 m) HYDICE sensors can uncover small man-made targets in a large image scene. As a result of such fine spatial resolution, only very few samples can be extracted for training in target detection and classification. The proposed band generation described above can be used to generate additional samples from a small pool of the training samples by making use of various nonlinear correlation functions, such as autocorrelation and cross-correlation.

In order to detect and classify targets in an unknown image scene, an unsupervised OSP algorithm developed in [28]–[30], called automatic target detection and classification algorithm (ATDCA) is used. Compared to the OSP classifier in [1], [2], the ATDCA does not require *a priori* knowledge of the image scene. It can be used to detect anomalies in an unknown image scene [28], a task that cannot be accomplished by the OSP, which needs the complete knowledge of the signatures present in the image scene. The ATDCA is an unsupervised OSP-based approach and is used in conjunction with the band generation to derive a new unsupervised target detection and classification approach, referred to as a generalized OSP (GOSP) hereafter. The effectiveness of the GOSP is then evaluated by experiments using SPOT and Landsat TM data. The results demonstrate that the GOSP significantly improves the OSP and is also comparable to the KFLM-based classifier proposed in [8]–[10].

The remainder of this paper is organized as follows. Section II reviews the OSP classifier developed in [1]. Section III presents a band generation process (BGP), which produces new additional bands from the original multispectral bands. Section IV briefly describes the implementation of the ATDCA used for an unsupervised classifier in the GOSP. Section V presents the GOSP approach, which combines the BGP with the ATDCA to achieve unsupervised target detection and classification. Section VI conducts a set of experiments to evaluate the classification performance of the GOSP. Section VII concludes some comments.

II. Orthogonal Subspace Projection Classifier

A. Hyperspectral Image Classification

A widely used approach to hyperspectral mixed pixel classification is linear unmixing [11]–[20], which has been studied extensively in the past, particularly by several leading groups such as University of Washington, Seattle, [14]–[18], Brown University, Providence, RI, [19], the University of Colorado, Boulder, [20], and the University of Reading, Reading, U.K., [13]. It models a mixed pixel vector as a linear mixture of endmembers (i.e., component constituents) resident in the pixel and the spectrum of the mixed pixel vector is a linear combination of endmembers' signatures so that individual endmembers in this linear mixture can be quantified and discriminated by inverting the endmember signature matrix. More precisely, let $\mathbf{r}_i$ be the spectral signature of the ith pixel vector in a hyperspectral image represented by an $l \times 1$ column vector, where l is the total number of spectral bands. Assume that M is an $l \times p$ endmember signature matrix, denoted by $(\mathbf{s}_1 \mathbf{s}_2 \cdots \mathbf{s}_p)$ where $\mathbf{s}_j$ is an $l \times 1$ column vector represented by the spectral signature of the jth endmember resident in the image scene $\mathbf{r}_i$, and p is the number of endmembers. Let α_i be a $p \times 1$ abundance column vector associated with $\mathbf{r}_i$ given by $(\alpha_{i1} \alpha_{i2} \cdots \alpha_{ip})^T$, where α_{ij} denotes the abundance fraction of the jth signature in pixel vector $\mathbf{r}_i$.

A linear spectral mixture model for $\mathbf{r}_i$ is described by

$$\mathbf{r}_i = M\alpha_i + \mathbf{n}_i \tag{1}$$

where $\mathbf{n}_i$ is an $l\times 1$ column vector representing additive white noise with zero mean and covariance matrix $\sigma^2 I$, and I is the $l \times l$ identity matrix. Solving (1) for α_i is an inverse problem. A tutorial reference for spectral mixture analysis can be found [15]. Three comments are noteworthy.

1) Depending upon whether or not the constraints $\Sigma_{j=1}^{p}\ \alpha_{ij} = 1$ and $\alpha_{ij} \geq 0$ for $0 \leq j \leq p$ are imposed on (1), there are unconstrained or constrained approaches. Since the OSP is an unconstrained method, only unconstrained linear mixing problems are considered in this paper, we refer constrained problems to [11]–[13].
2) The signature matrix in (1) is generally assumed to consist of p single pure endmember signatures. However, they are very difficult to obtain in practice. This is particularly true when the signatures are extracted directly from an image scene with no precise knowledge of ground truth. Such a problem is important and has been recently investigated in [14], [16] and [19].
3) Due to the scope of this paper, the issue of the unique solution to (1) is not addressed here, but has been considered somewhere else. We refer to [13] and [15] for further interest.

B. Orthogonal Subspace Projection

If we rewrite model (1) as

$$\mathbf{r} = \mathbf{d}\alpha_p + U\gamma + \mathbf{n} \tag{2}$$

where the subscript i is suppressed, $\mathbf{d} = \mathbf{s}_p$ is a desired signature, and $U = (\mathbf{s}_1\mathbf{s}_2\cdots\mathbf{s}_{p-1})$ is the undesired endmember signature matrix comprising of the first $p = 1$ signatures. Here, we assume without loss of generality that the last signature is the desired signature $\mathbf{d}$ needed to be classified. Since U is separated from M, it is possible to find a projection operator to annihilate U from an observed pixel vector prior to classification. One such projector, denoted by $P_U^{\perp}$, is given by

$$P_U^{\perp} = I - UU^{\#} \tag{3}$$

where $U^{\#} = (U^TU)^{-1}U^T$ is the psudo-inverse of U, and the notation $\perp_U$ in $P_U^{\perp}$ indicates that the projector $P_U^{\perp}$ maps $\mathbf{r}$ into the space $\langle U\rangle^{\perp}$, the orthogonal complement of the space $\langle U\rangle$.

Now, by applying $P_U^{\perp}$ to model (2), we can eliminate the U and obtain a new spectral linear mixture model with only desired signature $\mathbf{d}$ present in $\mathbf{r}$

$$P_U^{\perp}\mathbf{r} = P_U^{\perp}\mathbf{d}\alpha_p + P_U^{\perp}\mathbf{n} \tag{4}$$

where the original noise has been suppressed to $P_U^{\perp}\mathbf{n}$.

Equation (4) represents a standard signal detection problem and can be solved by a matched filter [31], denoted by $M_{\mathbf{d}}$ using the matched signal $\mathbf{d}$. The operator $P_U^{\perp}$, coupling with $M_{\mathbf{d}}$, is called an orthogonal subspace classifier P_{OSP}, derived in [1] and denoted by

$$P_{\mathrm{OSP}} = M_{\mathbf{d}}P_U^{\perp} = \mathbf{d}^TP_U^{\perp}. \tag{5}$$

One comment is noteworthy. The idea of OSP is not new. Similar approaches using the linear spectral mixture model specified by (1) were also developed [13]–[20]. In particular, the foreground-background analysis (FBA), developed in [32], maximizes the contrast between two sets of foreground and background spectra while minimizing the spectral variability within each set and can be shown to be a special version of the OSP. The mixture tuned matched filtering [33] and the spectral matched filter [34] can be also viewed as different versions of the OSP.

III. Band Generation Process (BGP)

The success of the OSP classifier in hyperspectral image classification is attributed to the fact that the projector $P_U^{\perp}$ in (3) rejects undesired signatures in U prior to application of a matched filter $M_{\mathbf{d}}$ specified by (5). In order for $P_U^{\perp}$ to effectively eliminate the undesired signatures, the intrinsic dimensionality q must be greater than or equal to p, the dimensionality of $\langle U\rangle$, where we assume that all signature vectors in M are linearly independent. Specifically, if all undesired signatures are mutually linearly independent, the intrinsic dimensionality must be at least equal or greater than p, i.e., $q \geq p$, where $p-1$ dimensions are used for undesired signatures and one dimension is reserved for $\mathbf{d}$. Otherwise, some undesired signatures will be blended and mixed into the space $\langle U\rangle^{\perp}$. As will be shown in experiments, when the BNC is violated, this unwanted signature mixing corrupts the $\mathbf{d}$ used in the matched filter and further results in poor classification. When this happens, either the dimensionality of $\langle U\rangle$ must be reduced to satisfy the BNC or the BNC must be relaxed. The former case can be done by eliminating unwanted signatures so that the data dimensionality can be reduced before the classification takes place. One such approach was reported in [8], [9], where some undesired signatures were considered to be interferers and were eliminated from the undesired signatures space $\langle U\rangle$ to reduce the dimensionality of $\langle U\rangle$. Under this circumstance, we need to know which signatures in U are interferers with respect to the desired signature $\mathbf{d}$ to achieve an optimal selection. In order to do so, we must exhaust all possible combinations of undesired signatures where each combination must be examined to determine which is the best case for the optimal performance. For instance, if $l < p-1$, there are $\binom{p-1}{l-1}$ combinations to remove undesired signatures from U. It is obviously not practical if $p-1$ is much greater than l. As an alternative to reduction of dimensionality of $\langle U\rangle$, we choose to increase the number of bands so that it is greater than $p-1$ as opposed to reduction of the number of signatures p to l. With this approach, there is no need to determine which signatures in U must be eliminated.

The idea of band generation process (BGP) arises from the fact that a second-order random process is generally specified by its first-order and second-order statistics. If we view the original bands as the first-order statistical images, we can generate a set of second-order statistical bands by capturing correlation between bands. These correlated images provide useful second-order statistical information about bands that is missing in the set of the original bands. The desired second-order statistics, including autocorrelation, cross-correlation, and nonlinear correlation can be used to create nonlinearly correlated images. The

concept of producing second-order correlated bands coincides with that used to generate covariance functions for a random process.

Let $\{B_i\}_{i=1}^{l}$ be the set of all original bands. The first set of second-order statistical bands are generated based on autocorrelation. They are constructed by multiplying each individual band by itself, i.e., $\{B_i^2\}_{i=1}^{l}$. A second set of second-order statistical bands are made up of all cross-correlated bands which are produced by correlating any pair of two different bands, i.e., $\{B_iB_j\}_{i,j=1,i\neq j}^{l}$. Adding these two sets of second order-statistics bands to $\{B_i\}_{i=1}^{l}$ produces a total of $l + l + \binom{l}{2} = (l^2+3l/2)$ bands. If more bands are needed, nonlinear functions may be used to generate so called nonlinear correlated bands. For example, we may use a square-root function to produce $\{\sqrt{B_i}\}_{i=1}^{l}$, or a logarithm function to produce $\{\log B_o\}_{i=1}^{l}$ to stretch out lower gray level values. In what follows, we describe several ways to generate second-order correlated and nonlinear correlated bands.

BGP:

Step 1) First-order band: $\{B_i\}_{i=1}^{l}$ is the set of original bands

Step 2) Second-order correlated bands:

(i) $\{B_i^2\}_{i=1}^{l}$ is the set of auto-correlated bands

(ii) $\{B_iB_j\}_{i,j=1,i\neq j}^{l}$ is the set of cross-correlated bands

Step 3) Nonlinear correlated bands:

(i) $\{\sqrt{B_i}\}_{i=1}^{l}$ is the set of bands stretched out by the square root.

(ii) $\{\log B_i\}_{i=1}^{l}$ is the set of bands stretched out by the logarithmic function.

It is worth noting that all the bands generated by the BGP are produced nonlinearly. These bands should offer useful information for classification because the classifier to be used for target detection and classification is linear and linearly generated bands will not provide useful information to help the classifier improve performance.

IV. Automatic Target Detection and Classification Algorithm (ATDCA)

In this section, the automatic target detection and classification algorithm (ATDCA) developed in [28]–[30] for an unsupervised OSP will be presented. The ATDCA will be included in the GOSP as an unsupervised classifier. It is important to note that no *a priori* knowledge is assumed for the GOSP. The idea of the ATDCA can be briefly described as follows.

There are two ways to get ATDCA started depending upon how an initial target, denoted by $\mathbf{T}_0$, is selected. If there is a desired target in the image scene, such as man-made objects provided by partial knowledge or visual inspection, this target can be chosen for the initial target $\mathbf{T}_0$. As a result, the ATDCA becomes desired target detection and classification algorithm (DTDCA) [30]. In this case, the DTDCA detects and classifies the desired target $\mathbf{T}_0$ in the image scene. In case there is no prior information available about the image scene, no target information can be used to find an initial target. Under this circumstance, we select a pixel vector with the maximum length as an initial target $\mathbf{T}_0$. In this case, $\mathbf{T}_0$ may not be a desired target and could be an interferer such as a scratch resulting from a sensor, rocks, etc. However, with this $\mathbf{T}_0$, the ATDCA can be initialized and

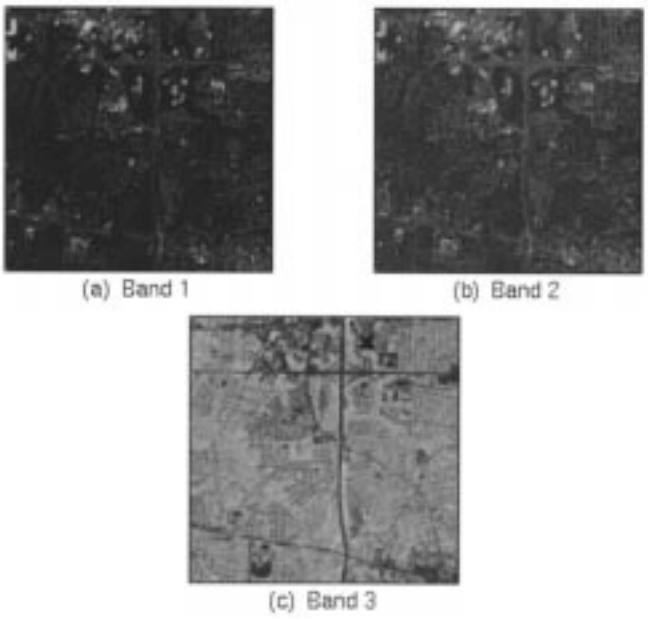

Fig. 1. Three-band SPOT images, band 1 (0.5–0.59 μm), band 2 (0.61–0.68 μm), band 3 (0.79–0.89 μm).

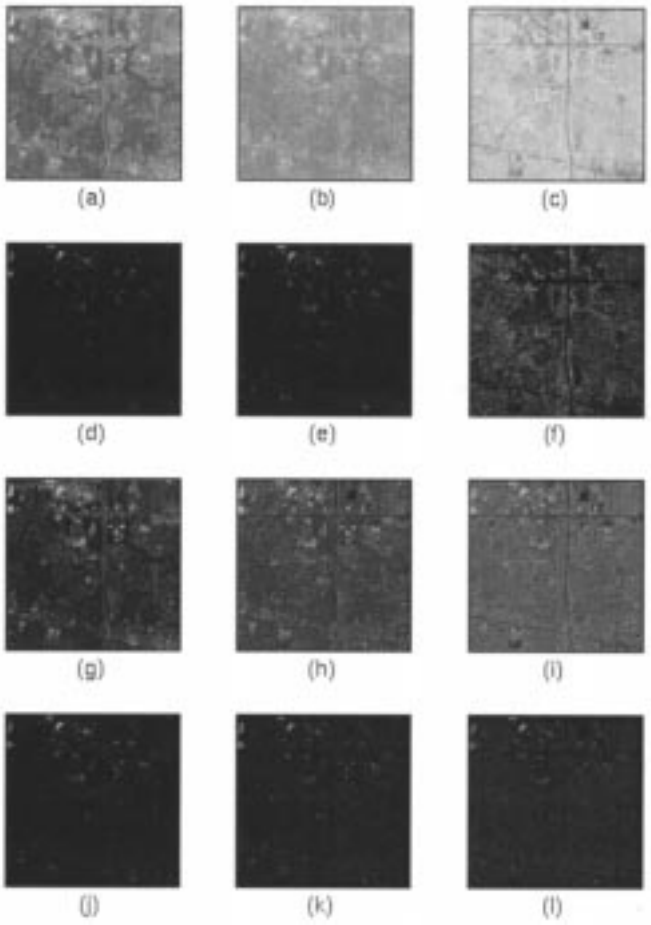

Fig. 2. 12 additional bands generated by the three SPOT bands.

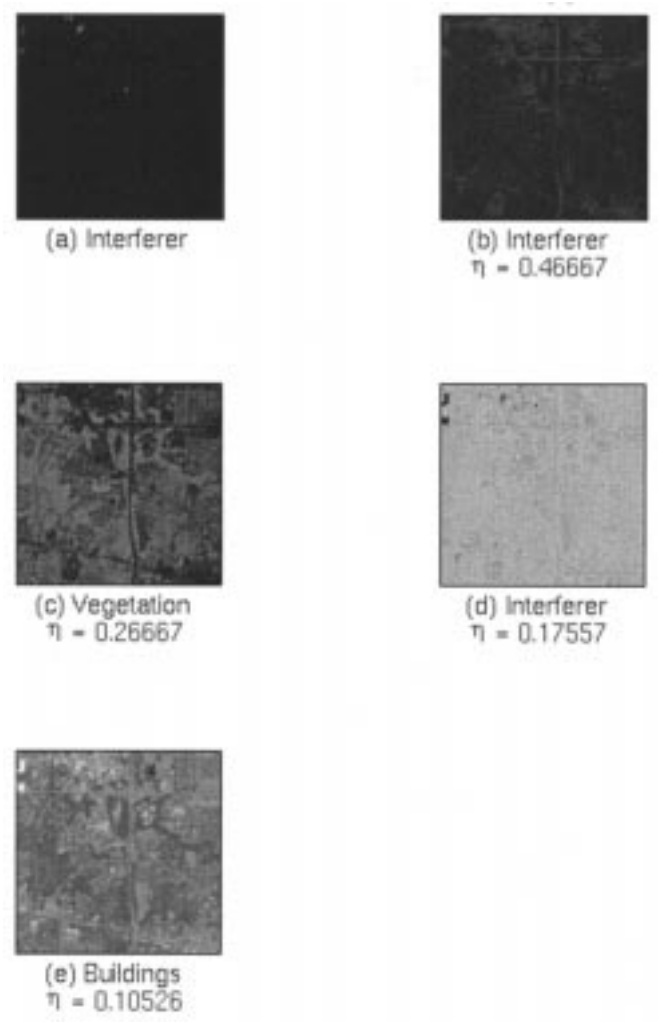

Fig. 3. Images classified by the ATDCA using five signatures.

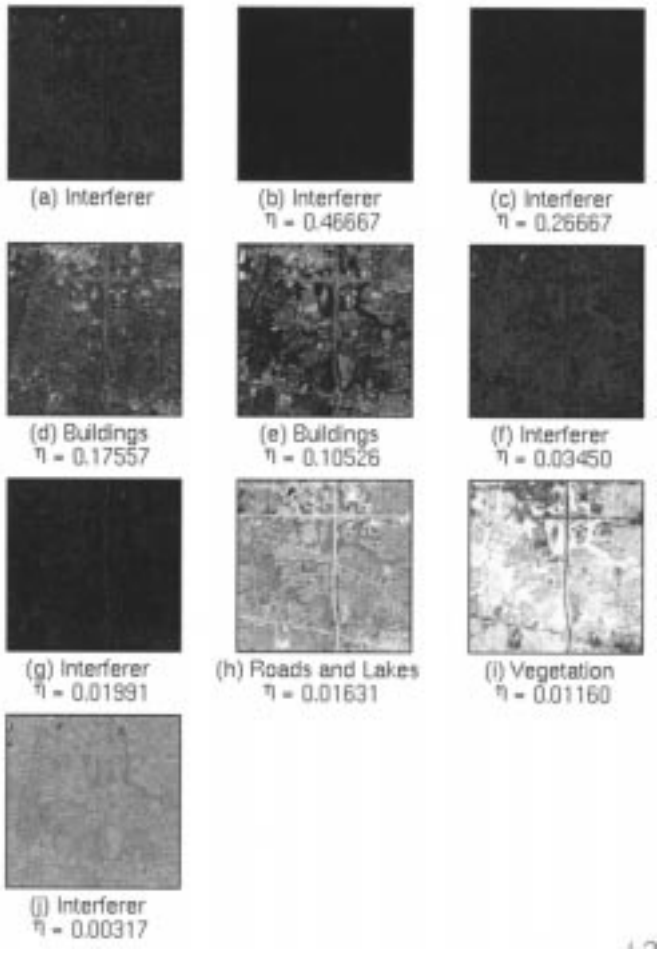

Fig. 4. Images classified by the ATDCA using ten signatures.

begins to generate new targets. Hopefully, all the potential targets will eventually be generated by the ATDCA.

After an initial target was chosen, the DTDCA and the ATDCA perform the same target generation process (TGP) as described below to generate additional targets. To the DTDCA, these newly generated targets will be considered to be interferers with respect to the desired target $\mathbf{T}_0$. For this reason, they must be eliminated before we classify $\mathbf{T}_0$. By contrast, the ATDCA assumes that no *a priori* knowledge is provided about the image scene. So, there are no desired targets and every generated target must be considered as a potential target and needs to be classified. Therefore, the ATDCA generally requires a data base or library to identify the detected and classified targets. The major difference between the DTDCA and the ATDCA is that the DTDCA only searches for the specific target $\mathbf{T}_0$ in the image scene while the ATDCA look for all possible targets in the image scene. As a consequence, the DTDCA generates only one fractional image for $\mathbf{T}_0$, whereas the ATDCA produces one separate fractional image for each of all targets generated by the TGP, including $\mathbf{T}_0$. This distinction results in different applications for the DTDCA and the ATDCA. The DTDCA can be used for reconnaissance applications where there is a specific target $\mathbf{T}_0$ of interest in an image scene. The ATDCA can be used for surveillance applications where it can be used to detect anomalies in an unknown image scene.

After $\mathbf{T}_0$ was determined, we need to find a target that is as distinct as possible from $\mathbf{T}_0$. One way to do so is to project all image pixel vectors by $P^{\perp}_{\mathbf{T}_0}$ via (3) into the space $\langle \mathbf{T}_0 \rangle^{\perp}$, the orthogonal complement space of $\langle \mathbf{T}_0 \rangle$ that is orthogonal to $\mathbf{T}_0$, then select the one with maximum length in the space $\langle \mathbf{T}_0 \rangle^{\perp}$ as the first target, denoted by $\mathbf{T}_1$ and detected in the image. In this case, $\mathbf{T}_1$ should have the most distinct features from $\mathbf{T}_0$. The difference between targets $\mathbf{T}_0$ and $\mathbf{T}_1$ is that $\mathbf{T}_1$ is unknown and can be only generated from orthogonal projection compared to $\mathbf{T}_0$, which could be selected by other means including partial knowledge. Then we assume that $\mathbf{T}_0$ is the desired signature and $\mathbf{T}_1$ is an undesired signature. By creating the first undesired target signature matrix U_1 specified by $U_1 = \mathbf{T}_1$, we calculate the orthogonal projection correlation index (OPCI) defined by $\text{OPCI}(\mathbf{T}_0, U_1) = \eta_1 = \mathbf{T}_0^T P^{\perp}_{U_1} \mathbf{T}_0$ to see if the algorithm needs to be continued by checking the value of the OPCI. The idea of using the OPCI as a stopping rule is to measure the residual of orthogonal projection resulting from the projection of $\mathbf{T}_1$ in the direction of $\mathbf{T}_0$. If $\text{OPCI}(\mathbf{T}_0, \mathbf{T}_1)$ is sufficiently small, the process of generating additional targets will be terminated. In this case, it passes on to the second stage for classification where an OSP classifier P_{OSP}, given by

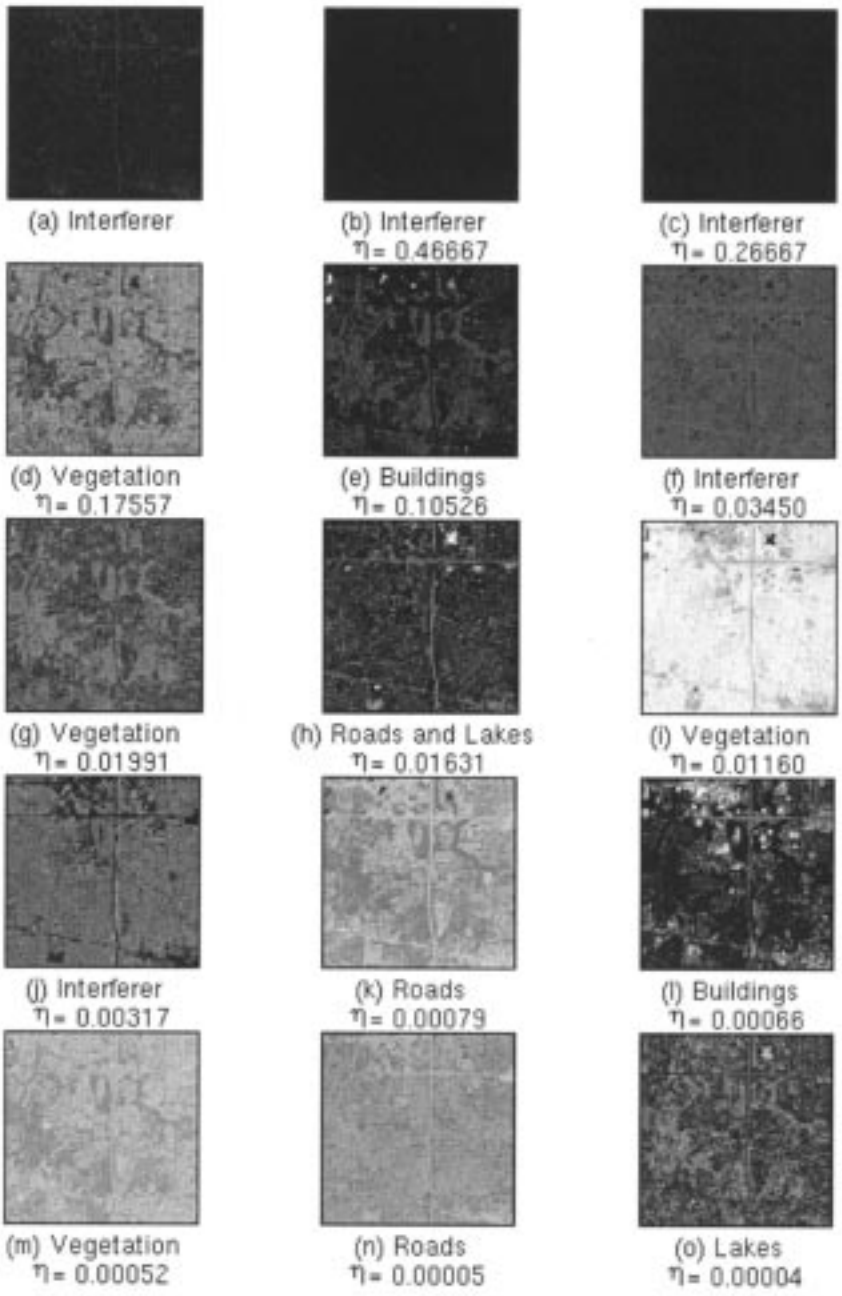

Fig. 5. Images classified by the ATDCA using 15 signatures.

(5), is applied to classify the detected targets $\mathbf{T}_0$ and $\mathbf{T}_1$. If OPCI$(\mathbf{T}_0, \mathbf{T}_1)$ is greater than a prescribed threshold ε, we continue the above process to generate a second target by applying $P^{\perp}_{(\mathbf{T}_0\mathbf{T}_1)}$ again to the original image. In this manner, all image pixel vectors are projected into a space $\langle \mathbf{T}_0, \mathbf{T}_1 \rangle^{\perp}$ orthogonal to the linear space spanned by the targets $\mathbf{T}_0$ and $\mathbf{T}_1$. As done before, the pixel vector with the maximum length in the space $\langle \mathbf{T}_0, \mathbf{T}_1 \rangle^{\perp}$ will be selected as a second target, denoted by $\mathbf{T}_2$. Then we calculate the OPCI between $\mathbf{T}_0$ and $U_2 = (\mathbf{T}_1\mathbf{T}_0)$ by $\eta_2 = \text{OPCI}(\mathbf{T}_0, U_2) = \mathbf{T}_0^T P^{\perp}_{U_2} \mathbf{T}_0$ with $U_2 = (\mathbf{T}_1\mathbf{T}_2)$ to determine if the target generation process should be terminated. The same procedure is repeated to find a third target, a fourth target, etc., until at the ith step, the OPCI$(\mathbf{T}_0, U_i)$ is small enough and less than ε.

Basically, the proposed ATDCA is a two-stage process. The first stage is the TGP to generate a number of potential targets in the image scene. It is then followed by an OSP-based classification process, target calssification process (TCP) where an OSP classifier is employed to classify all generated targets. The details of the ATDCA can described as follows.

Let $\{\mathbf{T}_1\mathbf{T}_2 \cdots \mathbf{T}_k\}$ be the kth target set generated at the kth step as well as the matrix $U_k = (\mathbf{T}_1\mathbf{T}_2 \cdots \mathbf{T}_k)$ formed by k targets with $\mathbf{T}_1$ as its first column vector, $\mathbf{T}_2$ as its second column vector, $\cdots$, $\mathbf{T}_k$ as its the last column vector. Then we define the OPCI between $\mathbf{T}_0$ and $U_k = (\mathbf{T}_1, \mathbf{T}_2 \cdots \mathbf{T}_k), \eta_k$ by

$$\eta_k = \text{OPCI}(\mathbf{T}_0, U_k) = \mathbf{T}_0^T P^{\perp}_{U_k} \mathbf{T}_0 \tag{6}$$

where $P^{\perp}_{U_k}$ is defined similarly by (3). Using OPCI given by (6) as a stopping rule, ATDCA can be summarized below. A block diagram is depicted in Diagram 1.

Automatic Target Detection and Classification Algorithm (ATDCA)

Stage 1. TGP

Step 1) Initial condition. Select a pixel vector with the maximum length as an initial target denoted by $\mathbf{T}_0$, i.e.,

$$\mathbf{T}_0 = \arg\{\max_{\mathbf{r}}[\mathbf{r}^T\mathbf{r}]\}. \tag{7}$$

Set $i = 1$ and $U_0 = \phi$

Step 2) Find the orthogonal projections of all image pixels with respect to $\mathbf{T}_0$ by using $P^{\perp}_{\mathbf{T}_0} = I - \mathbf{T}_0\mathbf{T}_0^{\#}$ where $\mathbf{T}_0^{\#} = (\mathbf{T}^T\mathbf{T}_0)^{-1}\mathbf{T}_0^T$ is the pseudo-inverse of $\mathbf{T}_0$.

Step 3) Select a first target in the space $\langle\mathbf{T}_0\rangle^{\perp}$, denoted by $\mathbf{T}_1$ by finding

$$\mathbf{T}_1 = \arg\{\max_{\mathbf{r}}[(P^{\perp}_{\mathbf{T}_0}\mathbf{R})^T(P^{\perp}_{\mathbf{T}_0}\mathbf{r}0]\}.$$

Step 4) If $\eta_1 = \mathbf{T}_0^T P^{\perp}_{U_1}\mathbf{T}_0 < \varepsilon$ with $U_1 = \mathbf{T}_1$, go to step 7. Otherwise, let $i = i+1$ and continue.

Step 5) Find the kth target $\mathbf{T}_k$ generated at the kth stage in the space $\langle\mathbf{T}_0, U_{k-1}\rangle^{\perp}$ with $U_{k-1} = (\mathbf{T}_1\mathbf{T}_2\cdots\mathbf{T}_{k-1})$, which is orthogonal to the space linearly spanned by the initial target $\mathbf{T}_0$ and the $k-$ 1st target set $\{\mathbf{T}_1\mathbf{T}_2\cdots\mathbf{T}_{k-1}\}$

$$\mathbf{T}_k = \arg\{\max_{\mathbf{r}}[(P^{\perp}_{(\mathbf{T}_0,U_{k-1})}\mathbf{r})^T(P^{\perp}_{(\mathbf{T}_0,U_{k-1})}\mathbf{r})]\} \tag{8}$$

where $P^{\perp}_{(\mathbf{T}_0,U_{k-1})}$ is defined by (3), $U = (\mathbf{T}_0, U_{k-1})$ is a matrix made up of $\mathbf{T}_0$, and $U_{k-1} = (\mathbf{T}_1\mathbf{T}_2\cdots\mathbf{T}_{k-1})$. Let $U_k = (\mathbf{T}_1\mathbf{T}_2\cdots\mathbf{T}_k)$ be the target matrix generated at the kth stage.

Step 6) Stopping rule: Calculate $\eta_k = \mathbf{T}_0^T P^{\perp}_{U_k}\mathbf{T}_0$ and compare it to the prescribed threshold ε. If $\eta_k > \varepsilon$, go to step 5. Otherwise, continue.

Step 7) At this point, the target generation process will be terminated. In this case, the set $\{\mathbf{T}_0, U_k\} = \{\mathbf{T}_0, \mathbf{T}_1, \cdots, \mathbf{T}_k\}$ will be the final target set used for the next stage of target classification.

Stage 2. TGP

In this stage, the target set $\{\mathbf{T}_0, \mathbf{T}_1, \cdots, \mathbf{T}_k\}$ represents all the targets that are assumed to be in the image and have been detected. Each of these targets is ready for classification.

Suppose that $\mathbf{T}_i$ is the ith target for $0 \le i \le k$. Let $\overline{U}_i = (\mathbf{T}_0, \cdots \mathbf{T}_{i-1}, \mathbf{T}_{i+1}, \cdots, \mathbf{T}_k)$ be the matrix consisting of all target signatures except the ith target signature $\mathbf{T}_i$. Apply the OSP classifier $P_{\mathrm{OSP}} = \mathbf{T}_i^T P^{\perp}_{\overline{U}_i}$ given by (5) to the image. The resulting fractional image will be the classification of the target $\mathbf{T}_i$.

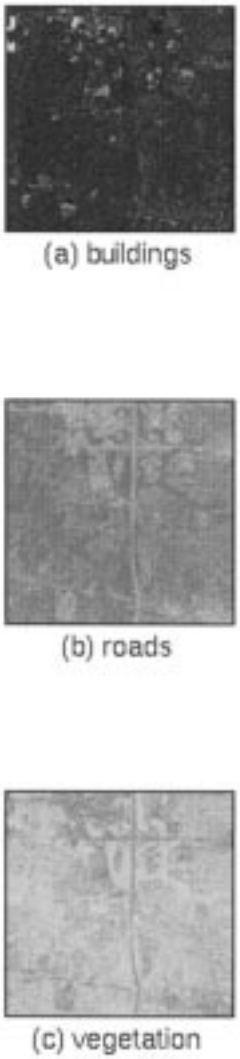

Fig. 6. Images classified by the OSP using (a) buildings, (b) roads, and (c) vegetation as signatures in the known signature matrix M.

It should be noted that each iteration from step 5 to step 6 in the TGP generates and detects one target at a time. The detected targets may not be significant and could be something else, for instance, clutter or background signatures or interfering signatures. This is due to the nature of the unsupervised TGP.

One comment on the OPCI is useful regarding the implementation of the ATDCA. The OPCI only provides a guide to terminate the ATDCA. Unfortunately, no optimal number of targets can be set in advance for the TGP to generate. This is determined by the prescribed error threshold ε used for the OPCI in step 6. It can be determined empirically. Another way to terminate the ATDCA is to preset the number of targets for generation. In this case, there is no need of step 6. Which one is a better approach depends upon different applications. It varies scene-by-scene.

V. Generalized Orthogonal Subspace Projection (GOSP)

The GOSP introduced in this section operates in two phases. The first phase implements the BGP to produce additional new bands from the original bands. The objective of the BGP is to

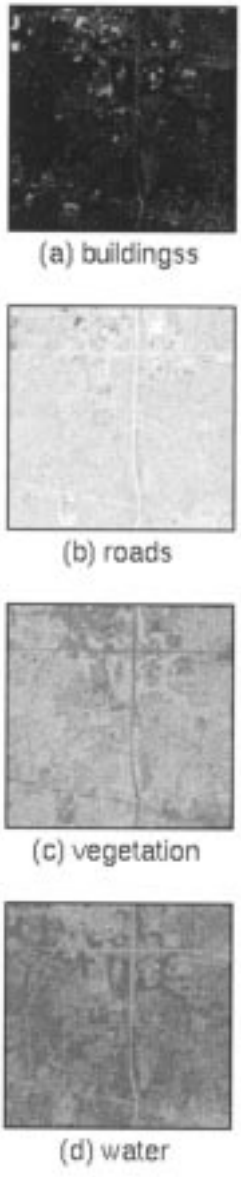

Fig. 7. Images classified by the OSP using (a) buildings, (b) roads, and (c) vegetation as signatures in the known signature matrix M.

make use of nonlinear correlation functions to produce a new set of second-order statistical bands. It is then followed by the second phase carried out by the ATDCA. The target detection and classification is accomplished unsupervisedly in this phase. The procedure to implement the GOSP is summarized as follows.

GOSP

Phase1) BGP

(i) Produce second-order correlated bands using auto-correlation or cross correlation functions.

(ii) Produce nonlinearly correlated bands using nonlinear functions, square root, or logarithm functions.

(iii) Form a new set of bands by including both original bands and bands generated by steps (i) and (ii).

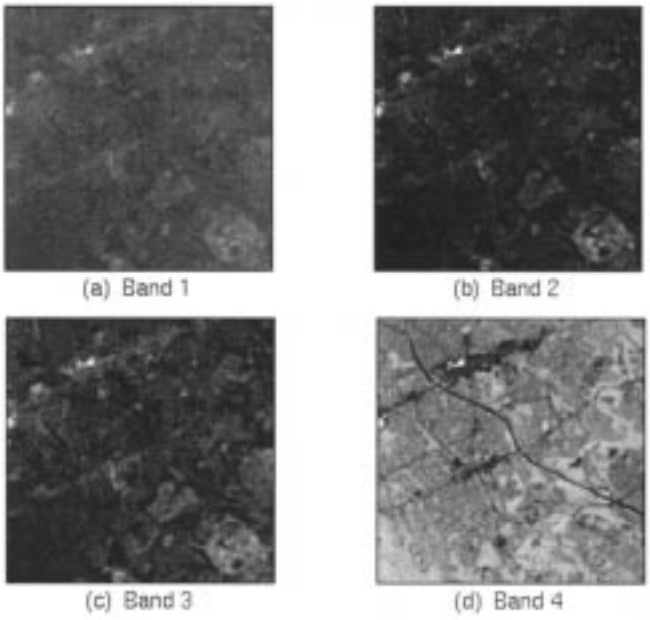

Fig. 8. Four-band Landsat thematic mapper (TM) images. (a) Band 1 (0.5–0.6 μm), (b) band 2 (0.6–0.7 μm), (c) band 3 (0.7–0.8 μm), and (d) band 4 (0.8–1.1 μm).

(2) ATDCA

i) Apply the TGP to the new set of bands produced by the BGP to generate a set of potential targets in the images.

ii) Apply the TCP to detect and classify the targets produced by the TGP.

VI. Experiments

Two sets of multispectral image data, SPOT and Landsat TM will be used to evaluate GOSP. The first set of image data were collected by the SPOT system in three spectral bands, two of which are from the visible region of electromagnetic spectrum referred to as band 1 (0.5–0.59 μm) and band 2 (0.61–0.68 μm), and the third band is from the near infrared region of electromagnetic spectrum referred to as band 3 (0.79–0.89 μm). The ground sampling distance (GSD) is 20 m. The second set of data are Landsat TM data. Due to unavailability of bands 5–7, only the first four bands were used for experiments, which are band 1 (0.45–0.52 μm), band 2 (0.52–0.60 μm), band 3 (0.63–0.69 μm), band 4 (0.76–0.90 μm), and a GSD of 30 m.

Example 1 (SPOT data): The three SPOT bands shown in Fig. 1 were taken over Northern Virginia where there are the Falls Church High School, the Little River Turnpike, a lake in the upper right of the image, and the Mill Creek Park. As shown in [8], the OSP did not work well in classifying four signatures, buildings, roads (parking lots), water, and vegetation. This is because there are only three bands available in the SPOT data, and OSP did not have enough dimensions for all four signatures for subspace projection. In this case, the BNC was violated. As expected, OSP performed poorly.

In order to relax the BNC, the autocorrelated, cross-correlated, and square root-based nonlinear-correlated bands were created as shown in Fig. 2 from the original three bands in

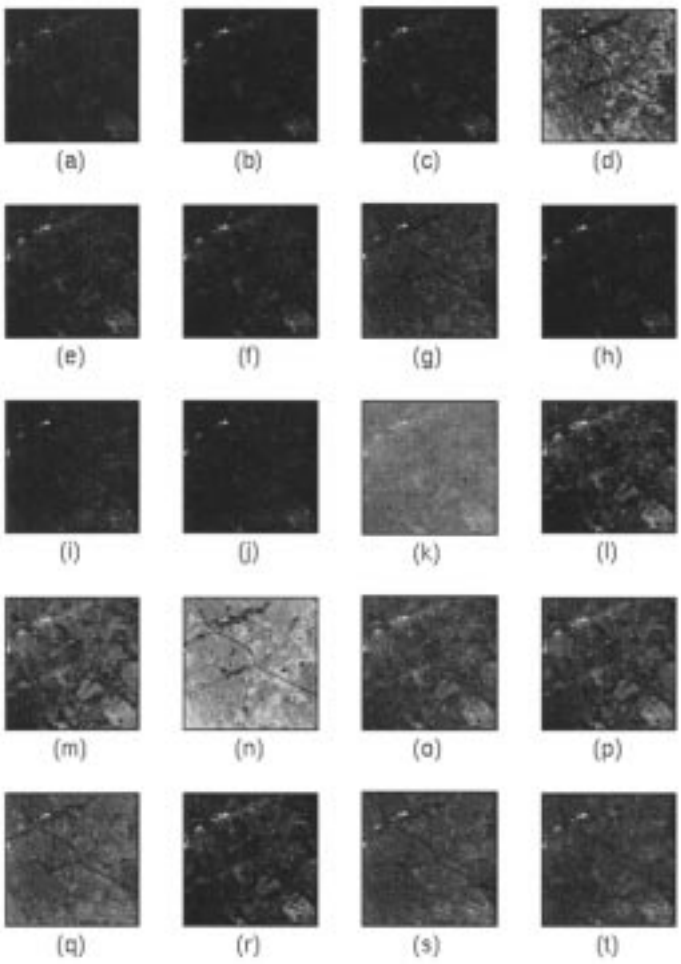

Fig. 9. 20 additional bands generated by the four TM bands in Fig. 8.

Fig. 1. The autocorrelated bands are labeled by Fig. 2(a)–(c), cross-correlated bands by Fig. 2(d)–(f), and square-root bands by Fig. 2(g)–(l). It should be noted that the square root function was applied to images in Fig. 1 and Fig. 2(d)–(f) to generate Fig. 2(g)–(l). We did not use the logarithmic function in this example to generate new bands since both square-root and logarithm have similar functions to stretch out the lower values of gray level. Combining images in Fig. 1 with images in Fig. 2 results in a total of 15 images. We then implemented the ATDCA using these 15 images and generated up to 15 target signatures. Figs. 3 –5 only show some representative results with the values of η given underneath each of the images. Fig. 3 was produced by the ATDCA using only five generated target signatures with OPCI $< \varepsilon = 0.075$. Figs. 4 and 5 are results of using 10 generated target signatures (with OPCI $< \varepsilon = 0.025$) and 15 target signatures (with OPCI $< \varepsilon = 10^{-5}$), respectively. As shown in Figs. 4 and 5, the results were better than that in Fig. 3 in terms of the classification of roads, buildings, water and vegetation. In particular, none of the images in Fig. 3 could classify the water lake. In Figs. 4(h) and 5(h) the water lake was detected along with roads, but the water lake extracted by Fig. 5(h) yielded the best result. It is interesting to note from Figs. 4 and 5 that using more target signatures for classification did not necessarily produce better results. This can be seen in Fig. 5, where the classification of vegetation was split into several images shown in Fig. 5(d), (g), (i), and (m), while only the image Fig. 4(i) shows vegetation. Similarly, the classification of roads was also split into the images shown in Fig. 5(h), (k) and (n), but only the image Fig. 4(h) shows the roads. This observation further provided evidence of the impact of the BNC. In hyperspectral image classification using more target signatures usually improves classification performance because there are hundreds of bands to accommodate a large number of target signatures that also include natural background signatures, interfering signatures and clutter [3]. However, as demonstrated above, using more signatures in multispectral imagery can sometimes deteriorate the classification performance as the number of signatures approaches the number of bands, i.e., $p \rightarrow l$, in which case, the BNC begins to show its effect on classification. According to our experiments, the best results were obtained with using signatures between 9 and 11.

In order to compare results produced by the GOSP, the OSP was also applied to the three-band SPOT images in Fig. 1 where three signatures: buildings, roads, and vegetation, and four signatures: buildings, roads, vegetation, and water were used as known signatures in the signature matrix M respectively. Figs. 6 and 7 show their respective classification results. The brighter spots extracted in Fig. 6(b) for roads classification turned out to

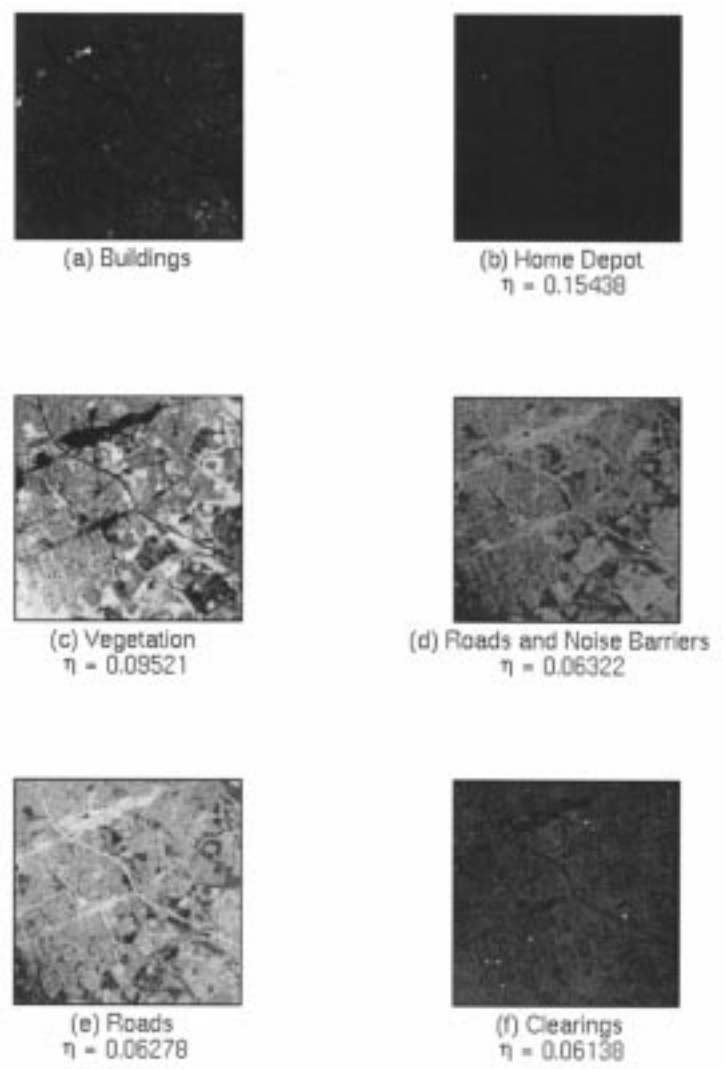

Fig. 10. Images classified by the ATDCA using six signatures.

be buildings not roads. Fig. 7(b) was supposed to classify roads, instead, both roads and the water lake were extracted. A similar problem was also observed in Fig. 7(d) where the image produced by the OSP for the water lake classification extracted buildings (brightest spots) and roads, but only barely detected the water lake. This is because the BNC is violated, i.e., $l = 3 < p = 4$. In this case, the rank of the signature matrix M cannot be greater than three. As a result, it had difficulty with classifying more than three signatures. Nevertheless, it should be noted that since the spectral signatures of the water lake and roads are very similar, the water lake and roads cannot be distinctly classified in all the cases [8]–[10]. This was also shown in Fig. 7(b) and (d) where buildings were also extracted in both images.

Example 2 (Landsat TM data): The four TM images shown in Fig. 8 were used in the following experiments. The scene was taken from the southern Baltimore area with the major state highway 695 running through from southeast to northwest, and the disc-shaped University of Maryland Baltimore County (UMBC), Baltimore, MD, campus on the bottom of the right corner. There are four local east-west roads, route 372, route 144, Edmondson Road, and U.S. Route 40 across the highway 695. Along the Route 40 east, and its junction with 695 is the site of the West View Shopping Mall.

Like Example 1, we generated additional bands based on the GOSP using autocorrelation, cross-correlation, and square-root function. A total of 20 new bands are created as shown in Fig. 9 where Fig. 9(a)–(d) are autocorrelated bands, Fig. 9(e)–(j) cross-correlated bands, Fig. 9(k)–(n) are bands resulting from taking the square-root of the images in Fig. 8 and Fig. 9(o)–(t) are resultant bands by taking the square-root of the images in Fig. 9(e)–(j). Once again, the logarithm function was not used in this example for band generation. So in this example, a total of 24 bands were used to classify various types of land covers in Fig. 8.

The ATDCA was applied to these images. Two experiments of interest are presented here where six target signatures (with OPCI $< \varepsilon = 0.005$) and 12 target signatures (with OPCI $< \varepsilon = 0.005$) were generated for illustration. Fig. 10 shows the images with six generated target signatures where the values of η are given underneath the images. Fig. 10(a) extracted buildings in the Mall and UMBC. It looks very similar to band 1.

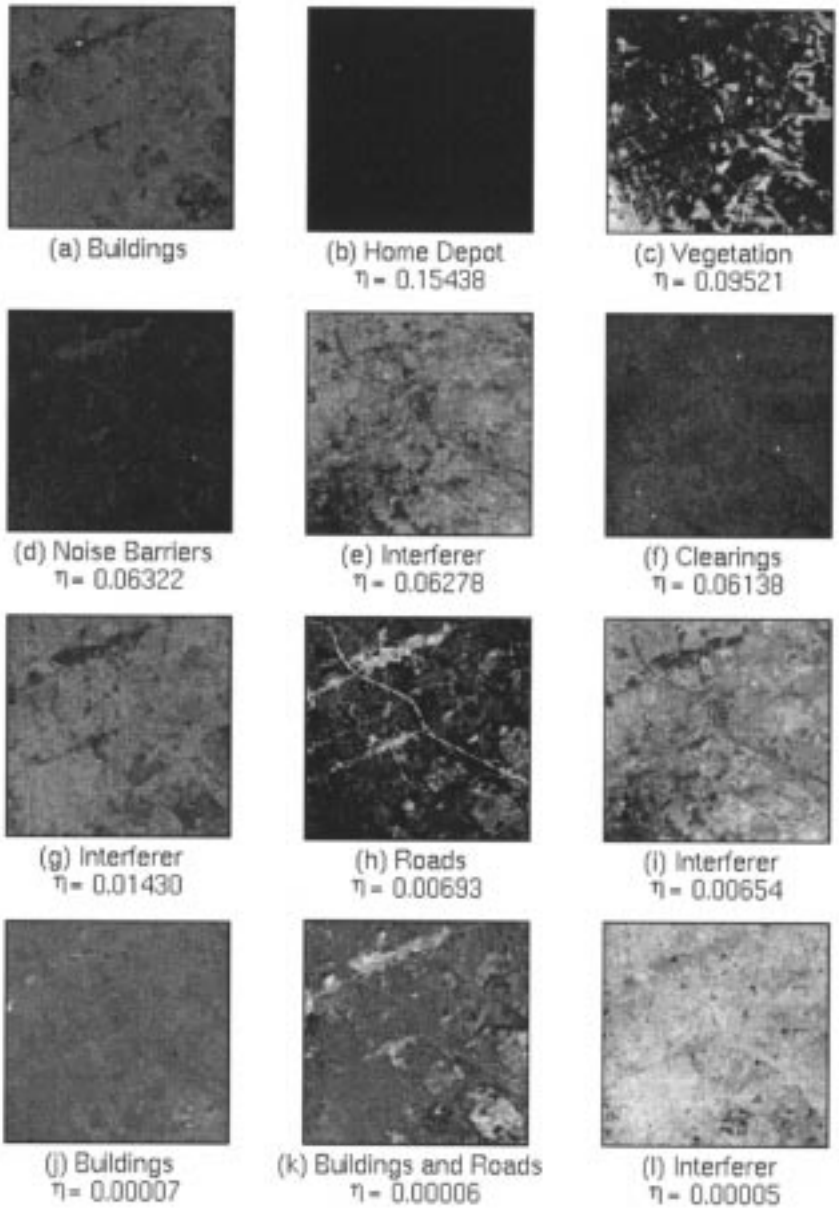

Fig. 11. Images classified by the ATDCA using 12 signatures.

Fig. 10(b) highlighted the brightest spot in band 1, which was the Home Depot store. Fig. 10(c) shows vegetation. Fig. 10(d) and (e) detected the major highway 695 and three roads where the buildings including the Mall along the route 40 east were also extracted. However, a bright spot right on the highway 695 shown in band 3 was picked up in Fig. 10(d). It was a construction site for installing noise barriers along the highway 695. If we examine band 1 carefully, there are six very dark spots in the image scene, which were singled out by the white spots in Fig. 10(f). They were clearings. Comparing Fig. 10 to Fig. 8 the images in Fig. 10 extracted most of the land cover information from all the four bands and each type of land cover was classified in different separate images. Fig. 11 shows 12 images produced by the ATDCA with the values of η given underneath the images where each image was the classification of one generated target signature. The results were not as good as Fig. 10. This is due to the fact that there were only a few types of land covers in the image scene. If the number of target signatures generated by the ATDCA is greater than the number of different types of land cover to be classified, it will result in a case that some type of land cover will be split into additional classes, thus they must be classified in separate images. Because of that, the classification performance in Fig. 11 was significantly reduced. For example, the buildings were split and classified by four images in Fig. 11(a), (h), (j), and (k), in which case the abundance fractions of buildings were distributed over these four images. So, the classification result of buildings was not as good as the image shown in Fig. 10(a).

If we apply the OSP directly to the four Landsat TM bands in Fig. 8 by using roads, buildings, and vegetation as signatures in the signature matrix M, the resulting images are shown in Fig. 12, where the images in Fig. 12(a)–(c) were the classifi-

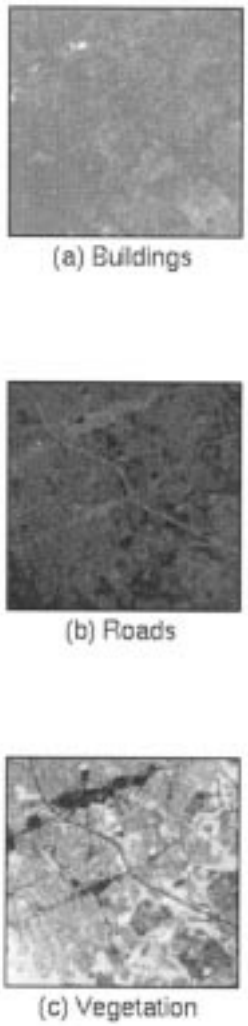

Fig. 12. Images classified by the OSP using (a) buildings, (b) roads, and (c) vegetation as signatures in the known signature matrix M.

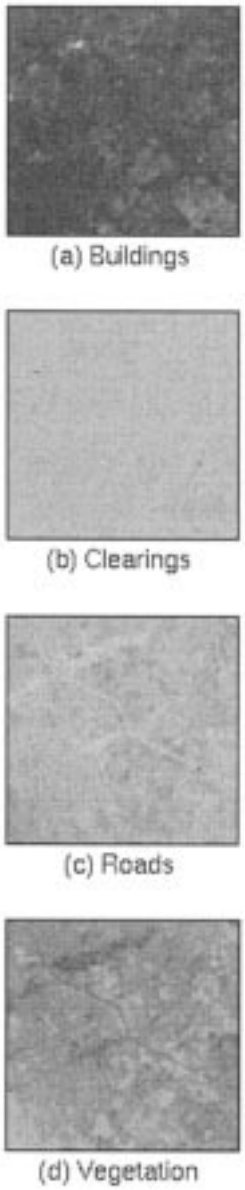

Fig. 13. Images classified by the OSP using (a) buildings, (b) roads, (c) clearings, and (d) vegetation as signatures in the known signature matrix M.

cation results of buildings, roads and vegetation respectively. Comparing Fig. 12 to Fig. 10, Fig. 10 outperformed Fig. 12. In particular, Fig. 10 detected six clearings, which were missed in Fig. 12. This example shows that the ATDCA can be used to detect anomalies in an image scene. Since there are four bands, we are allowed to have an additional target signature to be used to implement OSP. In this case, we extracted three bright spots in the bottom left of Fig. 10(f) as the target signature for clearings to make $p = 4$. The results shown in Fig. 13 were even worse than that in Fig. 12. This demonstration further shows the impact of the BNC on the performance of OSP.

It is worth noting that the additional images generated by band correlation can only provide second-order statistical information. They cannot be viewed the same as the bands acquired at different wavelengths. As a consequence, the number of such correlated bands required is generally much greater than the number of signatures to be classified. As shown in the above experiments, 12 additional images were generated from the three-band SPOT data and 20 for four-band TM data. However, it only required ten signatures for the SPOT and six signatures for TM data to produce good classification results. This is because the scene in the SPOT image is a national park that has at least four major types of land covers, buildings, roads (parking lots), water, and vegetation, while the urban area in TM images only shows three major signatures: buildings, roads, and vegetation, with no water in the TM image scene.

VII. Conclusion

When a multispectral image processing technique is applied to hyperspectral imagery, a common approach is to reduce data dimensionality. On the other hand, in applying a hyperspectral image processing technique, a general understanding is that it should be also applicable for multispectral imagery because the multispectral image classification seems to be a special case of hyperspectral image processing. As expected, one technique working for the latter should also work the former. Unfortu-

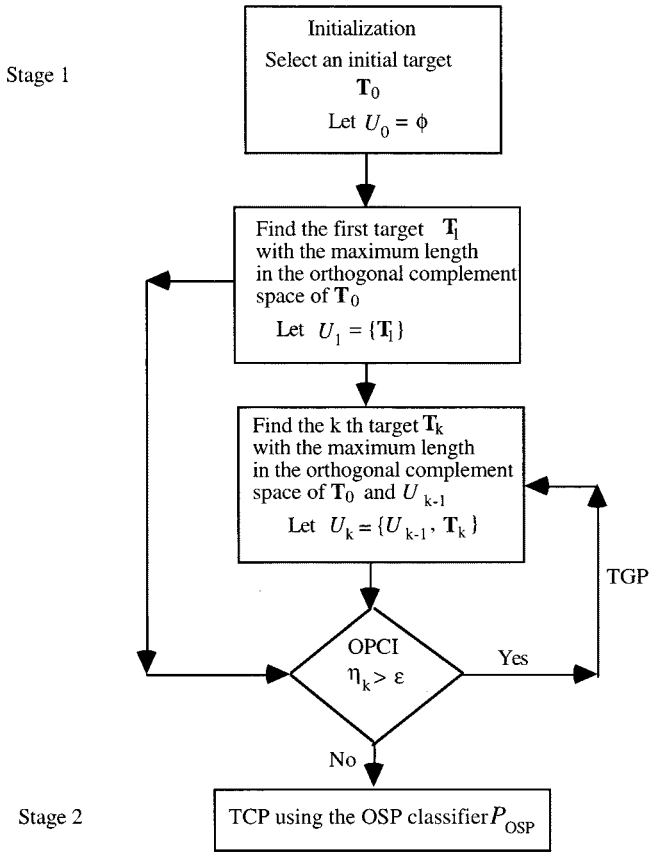

Diagram 1: Block diagram of ATDCA.

nately, this is generally not true. Despite the success of the OSP method in hyperspectral image analysis it does not necessarily guarantee that the same success can be also applied to multispectral imagery due to its IDC as demonstrated in this paper and [8]–[10]. This paper relaxed the IDC to the BNC and presented a GOSP to deal with multispectral image data. This is a very useful extension to the OSP. Unlike most of techniques seeking dimensionality reduction, the proposed GOSP takes an opposite approach by expanding bands of multispectral imagery. If the original bands are viewed as first-order statistical bands, the additional bands can be generated by the first-order statistical bands using second-order between-band correlation and nonlinear correlation, such as autocorrelation and cross-correlation. The idea of generating such correlated bands coincides with that used in second order random process where the auto-correlation and cross-correlation are used to capture second-order statistics of a process. Using these additional second-order statistical bands the BNC can be relaxed to make the OSP applicable to multispectral image classification. The experimental results demonstrate that the GOSP significantly improved the OSP performance in classification of SPOT and TM images. Recently, the ideas of the GOSP and the BGP were further applied to classification of magnetic resonance (MR) image sequences [35], [36] and the CEM method proposed in [2], [37]–[39]. The results of [35]–[39] provide evidence of the usefulness of the GOSP and the BGP in applications other than the one presented in this paper.

ACKNOWLEDGMENT

The authors would like to thank Dr. T. Foresman, Earth Laboratory, College of Engineering, University of Maryland Baltimore County (UMBC), Baltimore, MD, for providing Landsat TM data and Dr. S.-Y. Hsu, Susquehanna Resources and Environment, Inc., Binghamton, NY, for providing SPOT data. They would also like to thank A. Ifarragaerri for proofreading the manuscript. In particular, the authors would also like to express their appreciation to two anonymous reviewers, whose valuable comments greatly improved the quality and presentation of this paper.

REFERENCES

[1] J. C. Harsanyi and C.-I Chang, "Hyperspectral image classification and dimensionality reduction: An orthogonal subspace projection," *IEEE Trans. Geosci. Remote Sensing*, vol. 32, pp. 779–785, 1994.

[2] J. Harsanyi, "Detection and Classification of Subpixel Spectral Signatures in Hyperspectral Image Sequences," Ph.D. dissertation, Dept. Elect. Eng., Univ. Maryland Baltimore County, Baltimore, MD, Aug. 1993.

[3] C.-I Chang, T.-L. E. Sun, and M. L. G. Althouse, "An unsupervised interference rejection approach to target detection and classification for hyperspectral imagery," *Opt. Eng.*, vol. 37, pp. 735–743, Mar. 1998.

[4] T. M. Tu, C. H. Chen, and C.-I Chang, "A posteriori least squares orthogonal subspace projection approach to desired signature extraction and detection," *IEEE Trans. Geosci. Remote Sensing*, vol. 35, pp. 127–139, 1997.

[5] C.-I Chang, X. Zhao, M. L. G. Althouse, and J.-J. Pan, "Least squares subspace projection approach to mixed pixel classification in hyperspectral images," *IEEE Trans. Geosci. Remote Sensing*, vol. 36, pp. 898–912, May 1998.

[6] J. J. Settle, "On the relationship between spectral unmixing and subspace projection," *IEEE Trans. Geosci. Remote Sensing*, vol. 34, pp. 1045–1046, 1996.

[7] C.-I Chang, "Further results on relationship between spectral unmixing and subspace projection," *IEEE Trans. on Geoscience and Remote Sensing*, vol. 36, pp. 1030–1032, May 1998.

[8] C.-I Chang and C. Brumbley, "A Kalman filtering approach to multispectral image classification and detection of changes in signature abundance," *IEEE Trans. Geosci. Remote Sensing*, vol. 37, pp. 257–268, Jan. 1999.

[9] C. Brumbley, "An Unsupervised Linear Unmixing Kalman Filtering Approaches to Abundance Detection, Signature Estimation and Classification," Ph.D. dissertation, Dept. Comp. Sci. Elect. Eng., Univ. Maryland Baltimore County, Baltimore, MD, May 1998.

[10] C.-I Chang and C. Brumbley, "Linear unmixing Kalman filtering approach to signature abundance detection, signature estimation and subpixel classification for remotely sensed images," *IEEE Trans. Aerosp. Electron. Syst.*, vol. 37, pp. 319–330, Jan. 1999.

[11] Y. E. Shimabukuro and J. A. Smith, "The least-squares mixing models to generate fraction images derived from remote sensing multispectral data," *IEEE Trans. Geosci. Remote Sensing*, vol. 29, pp. 16–20, Jan. 1991.

[12] D. C. Heinz, C.-I Chang, and M. L. G. Althouse, "Fully constrained least squares-based linear unmixing," in *Int. Geosci. Remote Sensing Symp. '99*, Hanburg, Germany, June 28/July 2 1999, pp. 1401–1403.

[13] J. J. Settle and N. A. Drake, "Linear mixing and estimation of ground cover proportions," *Int. J. Remote Sensing*, vol. 14, no. 6, pp. 1159–1177, 1993.

[14] M. O. Smith, J. B. Adams, and D. E. Sabol, "Spectral mixture analysis—New strategies for the analysis of multispectral data," in *Image Spectroscopy—A Tool for Environmental Observations*, J. Hill and J. Mergier, Eds. Brussels, Belgium: ESC, 1994, pp. 125–143.

[15] J. B.] Adams, M. O. Smith, and A. R. Gillespie, "Image spectroscopy: Interpretation based on spectral mixture analysis," in *Remote Geochemical Analysis: Elemental and Mineralogical Composition*, C. M. Pieters and P. A. Englert, Eds. Cambridge, MA: Cambridge Univ. Press, 1993, pp. 145–166.

[16] D. E. Sabol, J. B. Adams, and M. O. Smith, "Quantitative sub-pixel spectral detection of targets in multispectral images," *J. Geophys. Res.*, vol. 97, pp. 2659–2672, 1992.

[17] A. R. Gillespie, M. O. Smith, J. B. Adams, S. C. Willis, A. F. Fischer, III, and D. E. Sabol, "Interpretation of residual images: Spectral mixture analysis of AVIRIS images," in *Proc. 2nd AVIRIS Workshop*, Owens Valley, CA, 1990, p. 243.

[18] J. B. Adams, M. O. Smith, and A. R. Gillepie, "Simple models for complex natural surfaces: A strateegy for hyperspectral era of remote sensing," in *Proc. IEEE Int. Geoscience and Remote Sensing Symp.'89*, Vancouver, BC, Canada, July, 10–14 1989, pp. 16–21.

[19] S. Tompkins, J. F. Mustarrd, C. M. Pieters, and D. W. Forsyth, "Optimization of endmembers for spectral mixture analysis," *Remote Sens. Environ.*, vol. 59, pp. 472–489, 1997.

[20] J. W. Boardman, "Inversion of imaging spectrometry data using singular value decomposition," in *Proc. IEEE Symp. Geoscience and Remote Sensing*, Vancouver, BC, Canada, July, 10–14 1989, pp. 2069–2072.

[21] H. Akaike, "A new look at statistical model identification," *IEEE Trans. Automat. Contr.*, vol. AC-19, pp. 716–723, 1974.

[22] M. Wax and T. Kailath, "Detection of signals by information theoretic criteria," *IEEE Trans. Acoust., Speech, Signal Processing*, vol. ASSP-33, pp. 387–392, 1985.

[23] J. rissnan, "Modeling by shortest data description," *Automatica*, vol. 14, pp. 465–471, 1978.

[24] J. Harsanyi, W. Farrand, and C.-I Chang, "Determining the number and identity of spectral endmembers: An integrated approach using Neyman-Pearson eigen-thresholding and iterative constrained RMS error minimization," in *Proc. 9th Thematic Conf. Geologic Remote Sensing*, Feb. 1993.

[25] C.-I Chang and Q. Du, "A noise subspace projection approach to determination of intrinsic dimensionality for hyperspectral imagery," in *EOS/SPIE Symp. Remote Sensing, Conf. Image and Signal Processing for Remote Sensing V*, Florence, Italy, Sept. 20–24, 1999, pp. 34–44.

[26] A. Papoulis, *Probability, Random Variables and Stochastic Processes*, 2nd ed. New York: McGraw-Hill, 1984, pp. 298–300.

[27] H. Ren, "A Comparative Study of Mixed Pixel Classification Versus Pure Pixel Classification for Multi/Hyperspectral Imagery," M.S. thesis, Dept. Comp. Sci. Elect. Eng., Univ. Maryland Baltimore County, Baltimore, MD, May 1998.

[28] H. Ren and C.-I Chang, "A computer-aided detection and classification method for concealed targets in hyperspectral imagery," in *Int. Symp. Geoscience and Remote Sensing '98*, Seattle, WA, July 5–10, 1998, pp. 1016–1018.

[29] ——, "A generalized orthogonal subspace projection approach to unsupervised multispectral image classification," in *SPIE Proc. SPIE Conf. Image and Signal Processing for Remote Sensing IV*, vol. 3500, Madrid, Spain, Sept. 21–25, 1998, pp. 42–53.

[30] C.-I Chang and H. Ren, "Automatic Target Detection and Classification in a Blind Environment," patent pending.

[31] H. V. Poor, *An Introduction to Signal Detection and Estimation*. New York: Springer-Verlag, 1994.

[32] M. O. Smith, D. A. Roberts, J. Hill, W. Mehl, B. Hosgood, J. Verdebout, G. Schmuck, C. Koechler, and J. B. Adams, "A new approach to quantifying abundances of materials in multispectral images," in *Proc. IEEE Int. Geosci. Remote Sensing Symp. '94*, Pasadena, CA, Aug. 1994, pp. 2372–2374.

[33] J. W. Boardman, "Leveraging the high dimensionality of AVIRIS data for improved sub-pixel target unmixing and rejection of false positive: Mixture tuned matched filtering," in *Summaries of 7th Annu. JPL Science Workshop*, vol. 1. Greenbelt, MD, 1998.

[34] I. S. Reed and X. Yu, "Adaptive multiple-band CFAR detection of an optical pattern with unknown spectral distribution," *IEEE Trans. Acoust., Speech, Signal Processing*, vol. 38, pp. 1760–1770, 1990.

[35] C. M. Wang, P. C. Chung, C.-I Chang, C.-W. Yang, and C. C. Chen, "An orthogonal subspace projection to MR image classification," in *4th Asian Conf. on Computer Vision*, Taipei, Taiwan, Jan. 2000.

[36] C. M. Wang, P. C. Chung, C.-I Chang, C.-C. Chen, and C.-S. Lo, "A constrained energy minimization approach to MR image classification," in *Proc. 12th IPPR Conf. Computer Vision, Graphics, and Image Processing*, Taipei, Taiwan, Aug. 1999, pp. 83–86.

[37] J.-M. Liu, C. M. Wang, C. M. Chieu, C.-I Chang, H. Ren, and C. W. Yang, "A generalized constrained energy minimization approach to subpixel detection for multispectral imagery," in *EOS/SPIE Symp. Remote Sensing, Conf. Image and Signal Processing for Remote Sensing V*, Florence, Italy, Sept. 20–24, 1999.

[38] C.-I Chang, J.-M. Liu, B.-C. Chieu, C.-M. Wang, C. S. Lo, P.-C. Chung, H. Ren, C.-W. Yang, and D.-J. Ma, "A generalized constrained energy minimization approach to subpixel target detection for multispectral imagery," *Opt. Eng.*, vol. 39, May 2000.

[39] J. C. Harsanyi, W. Farand, and C.-I Chang, "Detection of subpixel spectral signatures in hyperspectral image sequences," in *Annu. Meeting, Proc. American Society of Photogrammetry and Remote Sensing*, Reno, NV, 1994, pp. 236–247.

Hsuan Ren (S'98) received the B.S. degree in electrical engineering from the National Taiwan University, Taipei, Taiwan, in 1994, and the M.S. and Ph.D. degrees in electrical engineering from the University of Maryland Baltimore County (UMBC), Baltimore MD, in 1998 and 2000, respectively.

He is currently a Research Associate in the Remote Sensing, Signal and Image Processing Laboratory, UMBC. His research interests include data compression, signal and image processing, and pattern recognition. He is also a member of Phi Kappa Phi.

Chein-I Chang (S'81–M'87–SM'92) received the B.S., M.S., and M.A. degrees from Soochow University, Taipei, Taiwan, the Institute of Mathematics at National Tsing Hua University, Hsinchu, Taiwan, and the State University of New York, Stony Brook, respectively, all in mathematics, in 1973, 1975, and 1977. He also received the M.S. and M.S.E.E. degrees from the University of Illinois, Urbana, both in 1982, and the Ph.D. in electrical engineering from the University of Maryland, College Park, in 1987.

Since 1987, he has been with the Department of Computer Science and Electrical Engineering, University of Maryland Baltimore County (UMBC), Baltimore, MD, first as a Visiting Assistant Professor from January 1987 to August 1987, then as an Assistant Professor from 1987 to 1993, and currently as an Associate Professor. He was a Visiting Specialist with the Institute of Information Engineering, National Cheng Kung University, Tainan, Taiwan, from 1994 to 1995. He is on the editorial board of JOURNAL OF HIGH SPEED NETWORKS and is the Guest Editor of a special issue on TELEMEDICINE AND APPLICATIONS. His research interests include automatic target recognition, multispectral/hyperspectral image processing, medical imaging, information theory and coding, signal detection and estimation, and neural networks

Dr. Chang is a member of SPIE, INNS, Phi Kappa Phi, and Eta Kappa Nu.